



Contents lists available at ScienceDirect

Journal of Magnetism and Magnetic Materials

journal homepage: www.elsevier.com/locate/jmmm

Propagating vortices in ferrofluidic Couette flow under magnetic fields – Part II: Oblique orientated fields

Sebastian Altmeyer

Castelldefels School of Telecom and Aerospace Engineering, Universitat Politècnica de Catalunya, 08034 Barcelona, Spain

ARTICLE INFO

Keywords:

Taylor-Couette flow
Ferrofluid
Axial and transverse magnetic fields
Symmetry breaking
Propagating vortices

ABSTRACT

This work provides a numerical investigations of propagating vortex flow states (pVs) for ferrofluidic Couette flow with small aspect ratio and fixed non-rotating end-walls. The system is subjected to *oblique* magnetic fields as superposition of axial and transverse orientated fields. Such field configuration breaks the basic system symmetries and renders all flow structures to be inherently three-dimensional with complexer flow dynamics. Under oblique field configuration pV states are not direct present at onset. Instead oscillating flow states (oVs) bifurcate out of the stationary state. Basically these oVs hold same symmetries as pVs, which eventually evolve in a smooth transformation out of the oVs. pVs under oblique fields appear periodic or quasi-periodic, which render them topological speaking to exist on either two- or one-dimensional invariant manifolds as 2-torus or limit cycle (1-torus) solutions, respectively. In detail, structural modifications and changes in spatial and temporal behavior for pV solutions are studied with changing the magnetic field strength of the applied magnetic field.

1. Introduction

The flow between two concentric differentially rotating cylinders, the Taylor-Couette flow, has played a central role in the development of hydrodynamic stability theory [1–4] and has been a paradigm to investigate many fundamental nonlinear dynamical phenomena, pattern formation and self-organization. Its geometric allows for well-controlled experimental studies [5,6].

Considering realistic finite-size Taylor-Couette systems (TCS), the liquid is usually enclosed by the axial end walls at the top and bottom. Both, numerical and experimental works demonstrated that the resulting effects of these end walls are *not* negligible [22–27] even in the large aspect ratio TCS. The walls can thus have a *significant* effect on the flow dynamics.

A huge amount of literature in this area studied Taylor-Couette flow with a simple ‘classical’ fluid, and also with special focus on classical enclosed Taylor-Couette flow [1,3,4,6,28,29].

In recent years there has been an increasing amount of interest in the flow dynamics considering complex fluid as ferrofluids [20,21,7–19], which are manufactured fluids consisting of dispersion of magnetized nanoparticles in a liquid carrier. Consider ferrofluids [20,21], further parameters, such as the orientation of an applied magnetic field with respect to the fluid flow become important as this has crucial influence to the magnetoviscous effect in ferrofluids [30]. For example a symmetry-breaking transverse magnetic field modifies all flow structures in the TCS to become intrinsically three-dimensional [7,9,16].

Time dependent and propagating flow pattern are quite common in

TCS, e.g. most prominent primary bifurcating spiral vortices [5,31,6], or secondary bifurcating wavy Taylor vortices [32–34], etc. One common feature of these is the fact that they typically incorporate an azimuthal motion, typically rotation. Instead flow pattern, such as propagating vortices (pVs) which only involve axial motion are more rare. For classical TCS and ferrofluidic flow under pure axial field such pVs are characterized as “ $M = 0$ ”-mode [35,10,37] solutions, bifurcating out of stationary, axisymmetric cellular states (nV), i.e. toroidally closed non-propagating vortices [36].

The current paper is the second of two parts studying the influence of propagating vortices under different magnetic field configuration. In the present study we focus on *oblique* magnetic fields as a superposition of *axial* and *transversal* magnetic fields. Both configurations, pure axial and pure transversal magnetic fields are studied in detail in the first part [37] with special focus on modification in system symmetries.

Although becoming fully three-dimensional, pV states under symmetry breaking transversal magnetic field keep their characteristics including pure axial motion and remaining topological speaking a limit cycle solution (1-torus) [37]. However, this changes under oblique magnetic field configuration. The superposition of axial and transversal magnetic fields introduces further mode coupling [7] which eventually result in the appearing of a secondary incommensurable frequency. This renders the flow to be only quasi-periodic and as such to live on a two dimensional invariant manifold, i.e. a 2-torus solution.

In addition the bifurcating time dependent solutions appearing in a pitchfork bifurcation out of the stationary states do not necessarily direct include any propagation. Instead they only involve an axial *oscillation*

<https://doi.org/10.1016/j.jmmm.2021.167788>

Received 7 July 2020; Received in revised form 9 December 2020; Accepted 14 January 2021

Available online 29 January 2021

0304-8853/© 2021 Elsevier B.V. All rights reserved.

close to onset, which changes with variation in field strength in a smooth transition into *propagating* vortex solutions. Such axially oscillatory flow state has been reported earlier in TCS for either classical fluid, numerical and experimental in [38,39] as well as ferrofluid under magnetic field [19].

The overall goal of this study (first and second part) is to expand the parameter range in which the pV states are existing, stable and unstable, and further to investigate the topology of these solutions in ferrofluids in the presence of different magnetic fields.

2. Methods

2.1. System setting and the Navier–Stokes equation

We consider a standard Taylor-Couette system (TCS) (Fig. 1) consisting of two concentric, independently rotating cylinders. Within the gap between the two cylinders there is an incompressible, isothermal, homogeneous, mono-dispersed ferrofluid of kinematic viscosity ν and density ρ . The inner and outer cylinders have radius R_i and R_o , and they rotate with the angular velocity ω_i and ω_o , respectively. Here, we consider rigid boundary conditions in the axial direction with stationary non-rotating lids and no-slip boundary conditions on the cylinders. The height-to-gap aspect ratio is fixed to $\Gamma = L/d = 4$. The system can be characterized in the cylindrical coordinate system (r, θ, z) by the velocity field $\mathbf{u} = (u, v, w)$ and the corresponding vorticity field $\nabla \times \mathbf{u} = (\xi, \eta, \zeta)$. The radius ratio of the cylinders, R_i/R_o is kept fixed at 0.5. A homogeneous oblique magnetic field $\mathbf{H} = H_x \mathbf{e}_x + H_z \mathbf{e}_z$ (Fig. 1) with an axial component H_z and transversal component H_x is considered. [H_z and H_x being the field strengths.] Length and time scales of the system are set by the gap width $d = R_o - R_i$ and the diffusion time d^2/ν , respectively. The pressure in the fluid is normalized by $\rho \nu^2/d^2$, and the magnetic field \mathbf{H} and the magnetization \mathbf{M} can be conveniently normalized by the quantity $\sqrt{\rho/\mu_0 \nu}/d$, with free space permeability μ_0 . These considerations lead to the following set of non-dimensionalized hydro-dynamical equations [13,41]:

$$\left(\partial_t + \mathbf{u} \cdot \nabla \right) \mathbf{u} - \nabla^2 \mathbf{u} + \nabla p = \left(\mathbf{M} \cdot \nabla \right) \mathbf{H} + \frac{1}{2} \nabla \times \left(\mathbf{M} \times \mathbf{H} \right), \nabla \cdot \mathbf{u} = 0. \quad (1)$$

On the cylindrical surfaces, the velocity fields are given by $\mathbf{u}(r_i, \theta, z) = (0, Re_i, 0)$ and $\mathbf{u}(r_o, \theta, z) = (0, Re_o, 0)$, where the inner and outer Reynolds

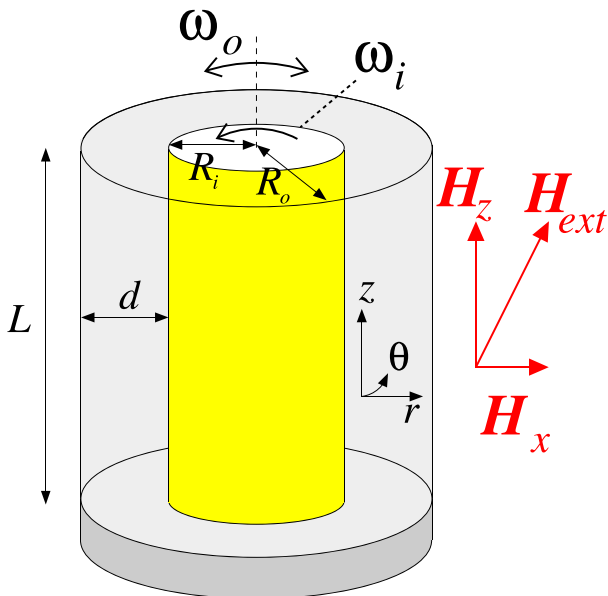


Fig. 1. Schematic of the Taylor-Couette system (TCS) with an external applied, oblique orientated homogeneous magnetic field $\mathbf{H}_{ext} = H_x \mathbf{e}_x + H_z \mathbf{e}_z$.

numbers are $Re_i = \omega_i r_i d/\nu$ and $Re_o = \omega_o r_o d/\nu$, respectively, where $r_i = R_i/(R_o - R_i)$ and $r_o = R_o/(R_o - R_i)$ are the non-dimensionalized inner and outer cylinder radii, respectively. In the present work we consider counter-rotating cylinders and therefore keep them fixed to $Re_i = 195$ and $Re_o = -300$, respectively, giving a rotation ratio $Re_o/Re_i \approx -1.54$.

Eq. (1) is to be solved together with an equation that describes the magnetization of the ferrofluid. Using the approach of Niklas [40] (derived from the theory by Shliomis [20] under the assumption of a stationary magnetization) with a small value of $\|\mathbf{M} - \mathbf{M}^{eq}\|$ and small magnetic relaxation time τ : $|\nabla \times \mathbf{u}| \tau \ll 1$. (see Appendix in [37] for details) leads to the following ferrohydrodynamical equations.

$$\left(\partial_t + \mathbf{u} \cdot \nabla \right) \mathbf{u} - \nabla^2 \mathbf{u} + \nabla p_M = s_N^2 \left\{ \nabla^2 \mathbf{u} - \frac{4}{5} [\nabla \cdot (\mathbb{S} \mathbf{H})] - \mathbf{H} \times \left[\frac{1}{2} \nabla \times \left(\nabla \times \mathbf{u} \times \mathbf{H} \right) - \mathbf{H} \times \left(\nabla^2 \mathbf{u} \right) + \frac{4}{5} \nabla \times \left(\mathbb{S} \mathbf{H} \right) \right] \right\}, \quad (2)$$

\mathbb{S} is the symmetric component of the velocity gradient tensor [41,13]. Terms in Eq. (2) containing \mathbb{S} describe elongational flow effects incorporating agglomeration and particle–particle interactions [41,13]. The pre-factor 4/5 represents the value of the so-called transport-coefficient λ_2 , based on experimental observations [42,41]. p_M is the dynamic pressure incorporating all magnetic terms that can be expressed as gradients including the corresponding part of the Kelvin force $(\mathbf{M} \cdot \nabla) \mathbf{H}$ resulting from the equilibrium magnetization. Thus the effect of the magnetic field and the magnetic properties of the ferrofluid on the velocity field can be characterized by a single parameter, the magnetic field or the Niklas parameter [40]:

$$s_N^2 = s_x^2 + s_z^2, \quad (3)$$

with

$$s_x^2 = \frac{2(2 + \chi) H_x c_N}{(2 + \chi)^2 - \chi^2 \eta^2}, s_z^2 = H_z c_N. \quad (4)$$

Here, χ is the magnetic susceptibility of the ferrofluid, which can be approximated by Langevin’s formula [45], and the Niklas coefficient c_N depends on the properties of the ferrofluid and magnetic field [40,7]. s_x^2 corresponds to the ratio $\tilde{\eta}_r/\tilde{\eta}$ between magnetic rotational viscosity and viscosity in absence of any magnetic field [43,44,40,20]. $\tilde{\eta}_r$ reflects the fact that the magnetic volume force which tends to align the magnetic moments being fixed to the particle parallel to the magnetic field *hinders* the free rotation of the magnetic particles due to the local vorticity Ω of the fluid.

The ferrohydrodynamic system Eq. (2) is solved numerically with the code G1D3 [6]. G1D3 combines a finite difference method of second order in (r, z) and time (explicit) with spectral decomposition in θ . Further detail regarding the numerical approach to solving the equations is outlined in the Appendix of the first part of this study in [37].

In this paper we present results for oblique orientated magnetic fields ($s_x \in [0, 1], s_z \in [0, 1]$). These values/parameters correspond to moderate magnetic fields used in several experiments [46,8,9].

Worth to emphasize the limitation of the Niklas approximation, which results from the stationary case and for small deviations of the magnetization near equilibrium, from one relaxation equation with one relaxation time. Thus the relaxation into equilibrium is determined by a relaxation constant that can depend on the magnetic field. As already stated by Niklas [40], the basic assumption is that the time t identifying the time scale for dynamical changes of the flow is larger than 10^{-6} s.

2.2. Numerical methods

The ferrohydrodynamical equations of motion Eq. (2) can be solved

[7,12,13] by combining a standard, second-order finite-difference scheme in (r, z) with a Fourier spectral decomposition in θ and (explicit) time splitting. The variables can be expressed as

$$f(r, \theta, z, t) = \sum_{m=-m_{\max}}^{m_{\max}} f_m(r, z, t) e^{im\theta}, \quad (5)$$

where f denotes one of the variables $\{u, v, w, p\}$. For the parameter regimes considered, the choice $m_{\max} = 16$ provides adequate accuracy. We use a uniform grid with spacing $\delta r = \delta z = 0.02$ and time steps $\delta t < 1/3800$. For diagnostic purposes, we also evaluate the complex mode amplitudes $f_{m,n}(r, t)$ obtained from a Fourier decomposition in the axial direction:

$$f_m(r, z, t) = \sum_n f_{m,n}(r, t) e^{inkz}, \quad (6)$$

where $k = 2\pi d/\lambda$ is the axial wavenumber.

For code validation especially with respect to here studied pV states a comparison with experimental findings by Ilzig et al. [10] is presented in [37]. Further some reproduction and comparison towards experimental data are illustrated in the [Supplementary Materials](#).

2.3. Symmetries & nomenclature

The schematics in Fig. 2 illustrates the here studied parameter space ($s_x \in [0, 1], s_z \in [0, 1]$). As detailed discussed in the first part [37] a pure axial magnetic field preserves all basic system symmetries [7,8,37,16], while a transversal magnetic field destroys these. However, instead they are replaced by complexer discrete space–time symmetries [13,37]. For further details of these symmetries with respect to propagating vortices, we refer to [37]. Having an oblique magnetic field further increase the complexity in the flow structures and modifying the symmetries.

The propagating vortices itself can basically distinguished in two types of flow structures. First type, either with simultaneously appearing vortices near both lids, which thereafter are also simultaneously propagating contrarily towards mid-height where they eventually become annihilated. In the second type similar generation, propagation and annihilation can be observed, but with key difference that the dynamics is *not* symmetric in the upper and lower half of the system. Instead the dynamics is alternating between both, upper and lower system half. This

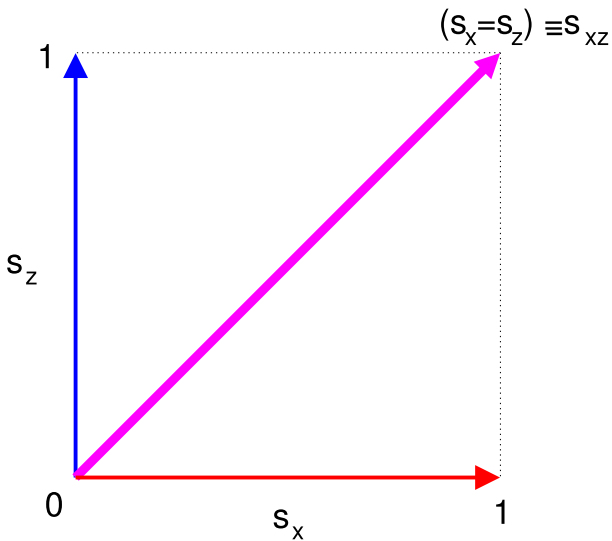


Fig. 2. Schematics illustrating the studied parameter space ($s_x \in [0, 1], s_z \in [0, 1]$). The present study crucially focus on the simultaneous variation of axial and transversal magnetic field strength $s_{xz} \equiv (s_x = s_z)$ (cf. [37] for pure axial and transversal fields.).

scenario is independent of any magnetic field and has been also observed for classical fluid in TCS [35]. For either pure axial and pure transversal fields it has been discussed in detail in the first part of this study [37]. There the corresponding solutions were identified/denoted as pV_2^S and pV_2^A (index 2 to characterize that the flows are fully 3D due to $m = 2$ stimulation under symmetry breaking transversal magnetic field [27,16]). However, these notation also include different specific symmetries (cf. [37]) which are not necessarily maintained under oblique field configuration. Thus, in order to avoid any confusion in this manuscript, we will describe the vortex solutions with symmetric appearance and dynamics as $oV_{2,1}^S$ [$pV_{2,1}^S$] and with asymmetric appearance and dynamics as $oV_{2,1}^A$ [$pV_{2,1}^A$], respectively. This only indicates the type of pV [oV] state without indication of any further system symmetries.

The index 2,1 identify all solutions present under oblique magnetic field, based on the fact that both $m = 2$ modes (also for pure transversal fields) and $m = 1$ modes are stimulated/finite under such applied magnetic fields [7,16].

Although the basic symmetries are destroyed under oblique field configuration, a complexer reflection $K_z^{H_x}$ about the annulus mid-height plane together with an inversion of the magnetic field direction, i.e reflection of both components axial and transversal at the same time, remains. Aside, given an aperiodic solution (with period τ), the flow field is also invariant under the discrete time translation Φ_τ . These symmetries read:

$$K_z^{H_x}(u, v, w, H_x, H_z)(r, \theta, z, t) = (u, v, -w, -H_x, -H_z)(r, \theta, -z, t) \quad (7)$$

$$\Phi_\tau(u, v, w, H_x, H_z)(r, \theta, z, t) = (u, v, w, H_x, H_z)(r, \theta, z, t + \tau). \quad (8)$$

Further, inverting only the axial field direction (cf. Section 2.3), $H_z \rightarrow -H_z$, while maintaining the other (transversal) one unchanged results in the appearance of a pair of *symmetry related solution*

$$K_z^{H_z}(u, v, w, H_x, -H_z)(r, \theta, z, t) = (u, v, w, H_x, H_z)^*(r, \theta, z, t) \quad (9)$$

This symmetry appears in phase space projection in (η_-, η_+) -plane as a reflection at the diagonal line $\eta_- = \eta_+$ (cf. gray colored curves in Fig. 5 which illustrate corresponding symmetry related solutions).

3. Results

3.1. Bifurcation dynamics

In absence of any magnetic field, the pV solution already has one characteristic frequency identifying it as limit cycle solution and as such to live on a one dimensional invariant manifold (1-torus). Although a pure transversal field breaks the basic system symmetries and renders all flows to be inherently 3D (due to stimulated $m = 2$ modes), it does not change the basic topological appearance of the propagating vortex solutions, the flow remains periodic and invariant only under complexer space–time symmetries (cf. [37,13]), keeping its limit cycle characteristics. This holds similarly for both, $pV_{2,1}^S$ and $pV_{2,1}^A$.

However, this changes for oblique field configuration. The superposition of transversal and axial field result in additional stimulated modes $m = 1$ (aside $m = 2$) [7,16]. As a result another incommensurable frequency may appear, which renders the flow (depending on various parameters) to exist on a two dimensional invariant manifold (2-torus). In the present study we focus on qualitative and quantitative analysis and underlying bifurcation scenario & sequences.

3.1.1. Bifurcation scenario and period time for s_{xz}

Following we will focus on oblique fields with identical magnetic field strength, $s_x = s_z$, which for simplicity we will denote as $s_{xz} \equiv (s_x = s_z)$.

The bifurcation diagram with s_{xz} is shown in Fig. 3, including an inset

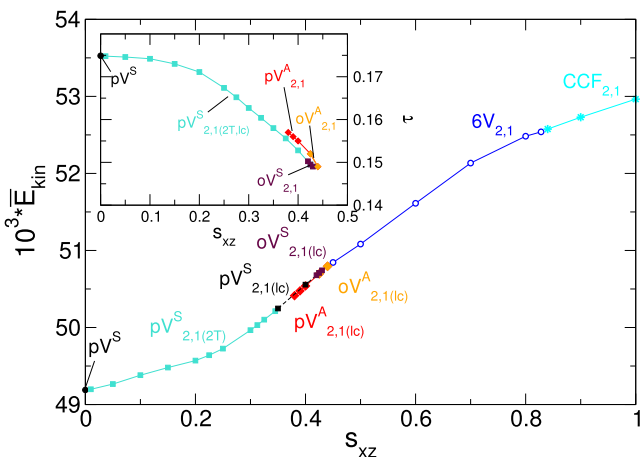


Fig. 3. Bifurcation diagram and time evolution. Bifurcation scenarios with s_{xz} . Shown is the total (time-averaged for time-dependent flow solutions) modal kinetic energy \bar{E}_{kin} (corresponding flow states are indicated). Solid [open] symbols indicate time dependent [stationary] solutions. The inset illustrates corresponding variation of period time τ with s_{xz} . Note, \bar{E}_{kin} for symmetric ($oV_{2,1}^S$, $pV_{2,1}^S$) and asymmetric ($oV_{2,1}^A$, $pV_{2,1}^A$) flow states are identical.

illustrating corresponding evolution in period time τ for the different flow states. At $s_{xz} = 0$ one finds the pure/classic *periodic* limit cycle solution pV^S [35,37], which becomes immediately destroyed as soon $s_{xz} \neq 0$ resulting in the only *quasi-periodic* 2-torus solution $pV_{2,1(2T)}^S$. With increasing the field strength, s_{xz} , the (time-averaged) modal kinetic energy \bar{E}_{kin} for $pV_{2,1(2T)}^S$ grows monotonously. At $s_{xz} \approx 0.33$ a frequency locking appears which result in a simpler limit cycle solution $pV_{2,1(lc)}^S$. Meanwhile \bar{E}_{kin} continuously grows with same slope as before. At $s_{xz} \approx 0.41$ the overall flow dynamics change significantly via a smooth transition into $oV_{2,1(lc)}^S$. This new flow state, $oV_{2,1(lc)}^S$, only involves an *oscillation* and *no propagating* of vortices anymore. Further increasing s_{xz} , $oV_{2,1(lc)}^S$ loses its stability at $s_{xz} \approx 0.43$ and moves transient towards $oV_{2,1(lc)}^A$ which is another oscillating solution, but with asymmetric/alternating dynamics instead. Increasing s_{xz} $oV_{2,1(lc)}^A$ disappears in the pitchfork bifurcation at $s_{xz} = 0.445$ leaving the stationary solution $6V_{2,1}$ behind. Worth to mention, that for even larger s_{xz} also $6V_{2,1}$ disappears and one finally finds the basic state $CCF_{2,1}$ (as described for classical fluid in [36]). On the other side, with decreasing s_{xz} , after $oV_{2,1(lc)}^A$ appears stable in the pitchfork bifurcation out of $6V_{2,1}$ it change in a smooth transient into the propagating vortex solution, $pV_{2,1(lc)}^A$. At $s_{xz} \approx 0.41$ before $pV_{2,1(lc)}^A$ eventually loses stability at $s_{xz} \approx 0.375$ and the flow moves transient towards $pV_{2,1(lc)}^S$. Further decreasing at $s_{xz} \approx 0.33$ the flow becomes quasi-periodic (2-torus solution) again, $pV_{2,1(2T)}^S$, while remaining stable until $s_{xz} = 0$. Worth to mention, that \bar{E}_{kin} of symmetric and asymmetric solutions $oV_{2,1(lc)}^S$ [$pV_{2,1(lc)}^S$] and $oV_{2,1(lc)}^A$ [$pV_{2,1(lc)}^A$], respectively, are identical (cf. [37] for details regarding the scenario in pure axial magnetic field).

In parallel, the corresponding period time τ behave just opposite and decreases monotonously with increasing s_{xz} before $oV_{2,1}^S$ [$oV_{2,1}^A$] vanishes (inset in Fig. 3). Similar behavior has been detected for pure axial and transversal magnetic fields, respectively, in part 1 [37] and moreover is in congruence with the well known stabilization effect of magnetic fields [40,7,8,8], the effective shift of the marginal stabilization threshold to larger control parameters. Recently Ilzig et al. [10] described this in their experimental study of pVs under pure axial magnetic field with one-side open boundary condition, as change (decrease) in orbital frequency of pVs with increasing field strength. Interestingly the period time τ for $o[p]V_{2,1}^S$ is slightly larger than the one

for $o[p]V_{2,1}^S$ at same parameters. Without going into detail we detected this small time difference to result from slightly different processes/dynamics at mid-height region. Here the central, mid-height region act as a defect structure, separating regions with different motion (here contrarily). More details regarding mechanism of separating defects can be found in [47].

General speaking, due to the stabilization effect, an increase in the magnetic field strength (shown for s_{xz} in Fig. 3, cf. Figs. 3 and 8 in [37] for pure axial and transversal magnetic fields), independent of the field direction has qualitative a similar effect as decreasing the inner cylinder rotation, $Re\ell_i$, as another control parameter [7,8].

3.1.2. Asymmetry with s_{xz}

For quantitative measure, Fig. 4 illustrates the asymmetry parameter $\eta_A = (\Delta\eta_+^2 - \Delta\eta_-^2)^{1/2}$ with $\Delta\eta_{\pm} = \max(\eta_{\pm}) - \min(\eta_{\pm})$ as already introduced in the first part [37]. Thus η_A measures the asymmetry regarding the diagonal $\eta_+ = \eta_-$. With increasing s_{xz} , the asymmetry parameter η_A grows for $pV_{2,1(2T)}^S$, whereby the slope continuously increases.

The significant change in the behavior of η_A at $s_{xz} \approx 0.31$ results from the topological change from being a quasi-periodic 2-torus solution, $pV_{2,1(2T)}^S$, towards a limit cycle (1-torus) solution, $pV_{2,1(lc)}^S$. This coincide with a drastic change in the area which the corresponding trajectory explore in phase space projection (cf. in (η_-, η_+) -plane in Fig. 5). Therefore η_A only decreases slightly with further increasing s_{xz} , a trend that remains unchanged through the smooth transition to $oV_{2,1(lc)}^S$. This decreasing characteristic in η_A with s_{xz} is significant stronger for the alternative propagating solution $pV_{2,1(lc)}^A$ and their smooth transition towards $oV_{2,1(lc)}^A$.

3.1.3. Phase Space with s_{xz}

In order to visualize the change and evolution in flow dynamics with variation in s_{xz} , Fig. 5 presents the phase portrait of $o[p]V^{(S,A)}$ solutions for different values s_{xz} over the (η_+, η_-) plane. Only the solution pV^S in absence of any magnetic field comes to lie on the diagonal $\eta_+ = \eta_-$ line, i.e. degenerated limit cycle [35,37]. The distance from the phase portraits to the diagonal line $\eta_+ = \eta_-$ is a measure of asymmetry, in particular of the degree to which Z_2 symmetry is broken. With increasing s_{xz} the trajectories of the 2-torus solution, $pV_{2,1}^S$, explore wider regions in phase space and move away (top left direction; color coded lines) from the diagonal line $\eta_+ = \eta_-$. By changing into a limit cycle solution

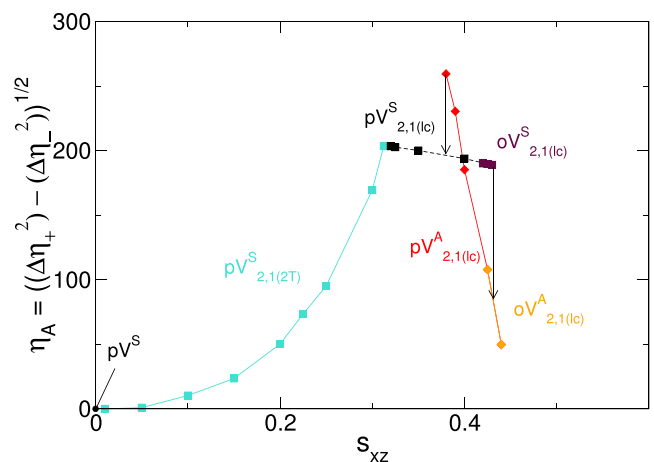


Fig. 4. Evolution of the asymmetry parameter η_A with s_{xz} for different oscillating and propagating vortex structures. The vertical arrows indicate the transition scenario when one solution loses stability and the flow moves transient towards another stable solution (see text for further details) (cf. Fig. 17 in [37] for pure transversal magnetic field).

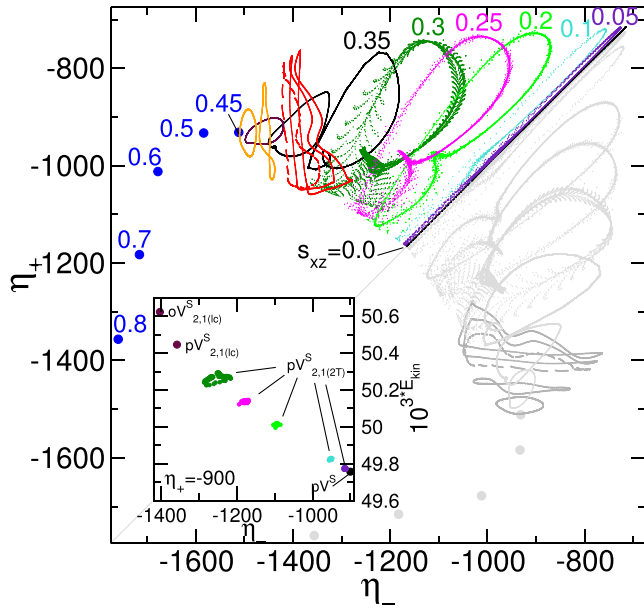


Fig. 5. Phase space projection for s_{xz} . Phase portraits of $oV_{2,1(lc)}^{(SA)}$ and $pV_{2,1(lc,2T)}^{(SA)}$ for field strength s_{xz} as indicated on (η_-, η_+) plane. Points correspond to stationary state $6 V_{2,1}$. Gray colored curves (below the diagonal line $\eta_+ = \eta_-$) show the corresponding symmetry related solution, which appear for inverting the axial field direction (cf. Section 2.3). They are mirrored with respect to the diagonal line $\eta_+ = \eta_-$. (Dark [Light] gray identify asymmetric [symmetric] states.) See Fig. 6 for more details and evolution of $oV_{2,1(lc)}^{(SA)}$ and $pV_{2,1(lc)}^{(SA)}$ close to onset. The inset shows the corresponding Poincaré section (E_{kin}, η_-) at $\eta_+ = -900$ (flow states are labeled).

$pV_{2,1(lc)}^S$ at $s_{xz} \approx 0.32$ the global flow dynamics simplifies and the limit cycle in the (η_+, η_-) plane continuously shrinks together. This behavior proceed throughout the smooth transition into $oV_{2,1(lc)}^S$, before ending in the stationary state $6 V_{2,1}$ (fixed point solution) at $s_{xz} \approx 0.445$. The alternating vortex solutions $oV_{2,1(lc)}^A$ and $pV_{2,1(lc)}^A$ only exist stable as limit cycle solution for here studied parameters. They feature the same behavior with approach to the onset/bifurcation point. Having reached the stationary state $6 V_{2,1}$ and further increasing s_{xz} initially the distance to the diagonal line $\eta_+ = \eta_-$ slightly increases, before it starts decreasing again. Thus for larger s_{xz} the flow moves towards a more symmetric appearance again.

The inset in Fig. 5 illustrates the corresponding two-dimensional Poincaré section (η_-, E_{kin}) at $\eta_+ = -900$ (same color code is used as in (η_+, η_-) plane). As mentioned before, being limit cycle solutions, corresponding curves/trajectories appear as single point, while the 2-torus solution appear one dimension higher as circles in (η_-, E_{kin}) . This characteristic is best visible for $s_{xz} = 0.3$ short before the disappearing of the 2-torus solution. See also [movie movie_pVA21_sxz03.avi](#) in SM.

The gray colored curves in Fig. 5 on the other side of the diagonal line $\eta_+ = \eta_-$ (right and down) illustrate the symmetry related solution, which appear for inverting the axial field direction (cf. Section 2.3), $H_z \rightarrow -H_z$, while maintaining the transversal one.

In order to see the flow dynamics more clear, Fig. 6 shows the evolution of $oV_{2,1(lc)}^{SA}$ and $pV_{2,1(lc)}^{SA}$ in phase space projection and Poincaré section for s_{xz} close to the onset (i.e. zoom in of Fig. 5). As discussed before, with decreasing s_{xz} $oV_{2,1(lc)}^S$ (stable at onset) and $oV_{2,1(lc)}^A$ (unstable at onset) bifurcate in the pitchfork bifurcation at $s_{xz} \approx 0.445$ which can be identified in phase space by the change from a single point towards the presence of a limit cycle. Therefore the corresponding Poincaré section at (E_{kin}, η_-) at $\eta_+ = -932$ (Fig. 6(b)) illustrates a single point for the limit cycle solutions. With decreasing s_{xz} , i.e. moving away from the onset, both flows smoothly change from oscillating to

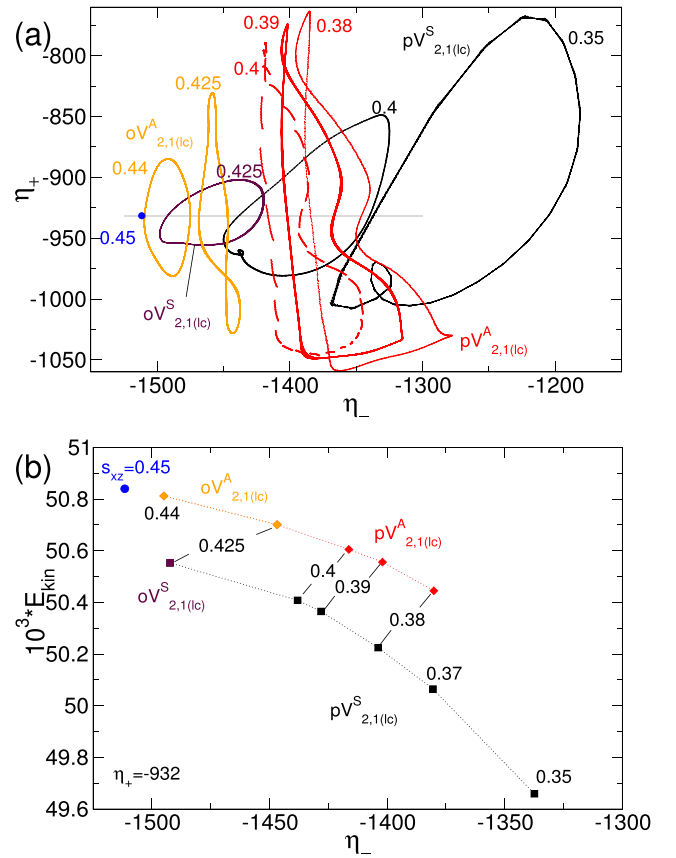


Fig. 6. As Fig. 5 but close to onset. (a) Phase portraits of limit cycle solutions, $oV_{2,1(lc)}^S$, $oV_{2,1(lc)}^A$, $pV_{2,1(lc)}^S$, $pV_{2,1(lc)}^A$ close to onset and for field strength s_{xz} on (η_-, η_+) and (b) corresponding Poincaré section (E_{kin}, η_-) at $\eta_+ = -932$ (cf gray horizontal line in (a)). Numbers in the figure identify the magnetic field strength s_x as indicated. ($\eta_+ = -932$ is chosen based on the stationary state $6 V_{2,1}$ for $s_{xz} = 0.45$).

propagating states and the trajectories explore wider region in phase. During this, E_{kin} monotonously decrease for both, while the energy for asymmetric/alternating solutions is always larger than those for symmetric ones.

Worth to mention, that we detected the smooth transition from oscillation towards propagating vortices and vice versa to appear at $s_{xz} \approx 0.41$ independent of symmetric $o[p]_{2,1(lc)}^S$ or alternating vortex solutions $o[p]_{2,1(lc)}^A$.

Fig. 7 illustrates the stationary solution $6 V_{2,1}$ at $s_{xz} = 0.45$, close to the onset out of which either $oV_{2,1(lc)}^A$ (stable) and $oV_{2,1(lc)}^S$ (unstable) appear, respectively. Mode amplitudes $|u_{m,n}|$ and radial flow $u(r, \theta)$ (Fig. 7(b, e)) highlight the complexer mode spectra, in particular the stimulated $m = 2$ modes (due to transversal magnetic field, cf. vector plot $[u(r, z), w(r, z)]$ for $\theta = 0$ and $\theta = \pi/4$ in Fig. 7(d)) and $m = 1$ modes (due to superposition of transversal and axial; i.e. oblique field).

3.2. Flow structures and transition scenarios

As discussed before only the asymmetric/alternating vortex solution $oV_{2,1(lc)}^A$ is stable at the onset $s_{xz} \approx 0.445$ and with decreasing s_{xz} first undergoes a smooth transition into $pV_{2,1(lc)}^A$ before eventually losing its stability at $s_{xz} \approx 0.33$ where the flow dynamics transfer into the symmetric vortex solution $pV_{2,1(lc)}^S$. Fig. 8 shed some light into this evolution and change in symmetry from different perspectives. The spacetime plots of $u(\theta, z)$ at mid-gap clearly indicates a change in the flow pattern.

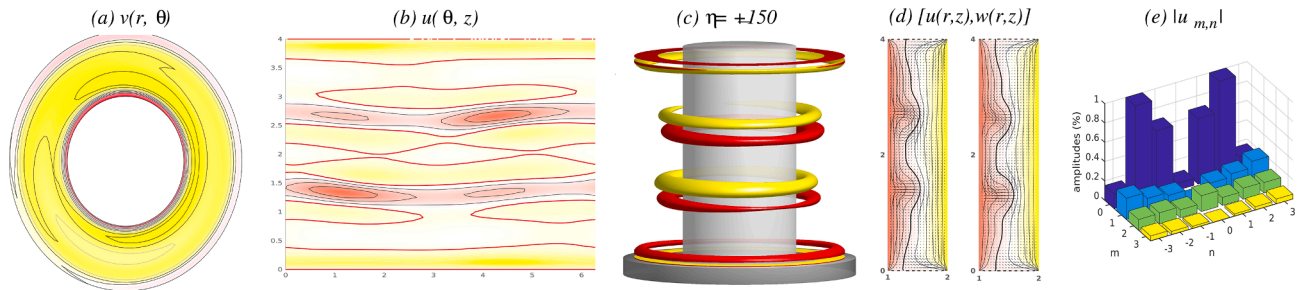


Fig. 7. Stationary $6 V_{2,1}$ flow structure for $s_{xz} = 0.45$. Shown are (a) the azimuthal velocity $v(\theta, z)$ at mid-height [red (yellow) color indicates positive (negative) flow], (b) the radial velocity $u(\theta, z)$ on an unrolled cylindrical surface in the annulus at mid-gap [red (yellow) color indicates in (out) flow], (c) isosurfaces of $\eta = \pm 150$ [red (dark gray) and yellow (light gray) colors correspond to positive and negative values, respectively, with zero specified as white] and (d) vector plot $[u(r, z), w(r, z)]$ (at left: $\theta = 0$ and right: $\theta = \pi/4$) of the radial and axial velocity components including color-coded azimuthal velocity v . (e) Mode amplitudes $|u_{m,n}|$ of the radial velocity field u over the $m-n$ -plane. The values are scaled regarding the maximum mode amplitude to be 1. [Analog visualizations are used in the following to characterize other flow structures in the paper.]

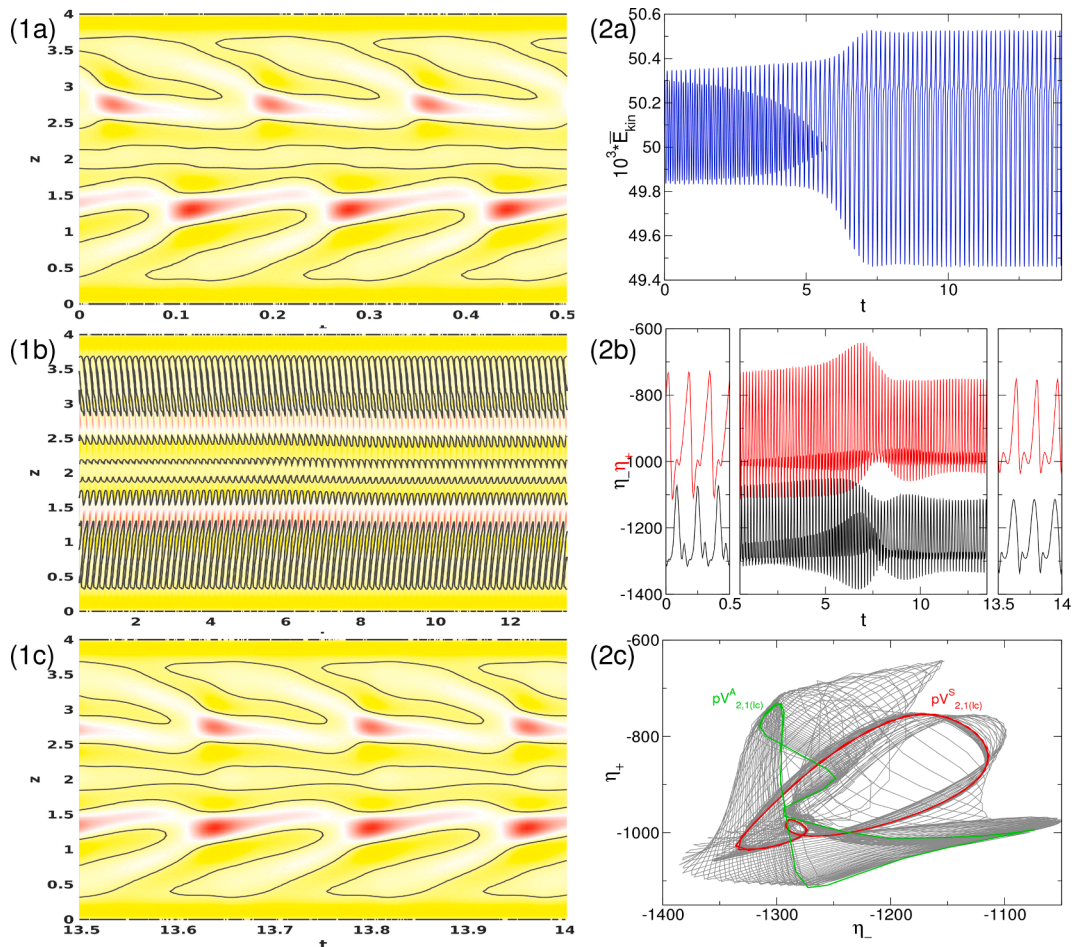


Fig. 8. Transition from $pV_{2,1(lc)}^A$ into $pV_{2,1(lc)}^S$ at $s_{xz} = 0.325$. (1) Space-time plot of $u(\theta, z)$ at radial position $r = r_i + d/2$ shown for different times during the transition: (a) $0 \leq t \leq 0.5$, (b) $0.5 \leq t \leq 13.5$, and (c) $13.5 \leq t \leq 14$. Red (dark gray) and yellow (light gray) correspond to positive and negative values. (2) Quantities of time series of (a) E_{kin} , (b) η_{\pm} and (c) phase portrait (η_{-}, η_{+}) illustrating the corresponding evolution of trajectories from $pV_{2,1(lc)}^A$ into $pV_{2,1(lc)}^S$.

At the beginning of the transformation ($pV_{2,1(lc)}^A$, Fig. 8(a)) the black zero contour lines as indicator for the propagating vortices, appear alternating (about half period shifted) near the upper and lower lids. The plot illustrates a kind of elliptic pattern pointing towards the mid-height region and to the right (due to time evolution). Contrary at the end of the transition scenario for $pV_{2,1(lc)}^S$ (Fig. 8(c)) the pattern illustrates a symmetric appearance at top and bottom of these elongated elliptic regions. Corresponding time evolution of local measures η_{+} and η_{-}

(Fig. 8(2b, 2c)) during the transition show the initial half period shift which becomes synchronized at the end $\eta_{+} = \eta_{-}$. The always present difference in absolute values η_{\pm} indicates the broken $K_z^{H_s}$ symmetry for oblique fields. Although the time-averaged averaged modal kinetic energy \bar{E}_{kin} is basically identical for $pV_{2,1(lc)}^A$ and $pV_{2,1(lc)}^S$ (Fig. 3), the variation over one period τ is significant larger in the case of the symmetric appearance $pV_{2,1(lc)}^S$ (8(2a)). In opposite manner the variation in η_{\pm} over one period shrinks during the transition to be smaller in $pV_{2,1(lc)}^S$

compared to $pV_{2,1(lc)}^A$ (Fig. 8(2b)). In the similar manner the phase portrait (η_+, η_-) elucidate the evolution from the asymmetric vortex solution $pV_{2,1(lc)}^A$, towards the symmetric vortex solution $pV_{2,1(lc)}^S$. The fact that the trajectories of both, $pV_{2,1(lc)}^A$ and $pV_{2,1(lc)}^S$, are far away from the diagonal line with $\eta_+ = \eta_-$ is a further indication for the asymmetric characteristic with respect to classical Z_2 symmetry.

For a direct comparison of the different types of flow states with either symmetric or alternative motion in upper and lower half of the cylinder, Figs. 9 and 10 show both oscillating solutions at $s_{xz} = 0.0425$, while Figs. 11 and 12 present the same for propagating states at $s_{xz} = 0.4$ after the smooth transition.

In general, 3D plots of the azimuthal vorticity, η , and the radial velocity $u(r, \theta)$ at cylinder mid-gap indicate the either symmetric motion (from lids towards mid-height) of vortices for $oV_{2,1(lc)}^S$ [$pV_{2,1(lc)}^S$] or the alternative appearance and motion of these vortices for $oV_{2,1(lc)}^A$ [$pV_{2,1(lc)}^A$] (Fig. 9 [11]). For all flow states, the dominant stimulated modes, i.e. $m = 2$ (due to the symmetry breaking transverse magnetic field) and $m = 1$ (due to superposition of axial and transversal magnetic field) are best visible in $u(r, \theta)$ (cf. stationary case for 6 $V_{2,1}$ presented in

Fig. 7). For more details and better impression regarding the dynamics and evolution over one period see corresponding movies [movie_pVS21_sx0425.avi](#), [movie_pVA21_sx0425.avi](#), [movie_pVS21_sx04.avi](#), and [movie_pVA21_sx04.avi](#) in SM. In case of the symmetric solutions, $oV_{2,1(lc)}^S$ and $pV_{2,1(lc)}^S$, respectively, the vortices appear to have the same strength/amplitude (vortex size) in upper and lower system half. In contrast for the alternating solutions, $oV_{2,1(lc)}^A$ and $pV_{2,1(lc)}^A$, the strength of the vortices in upper and lower system half is different. The propagating vortices are larger (cf. $u(r, \theta)$ in Figs. 9 and 11).

Although the averaged kinetic energy \bar{E}_{kin} for $oV_{2,1(lc)}^S$ [$pV_{2,1(lc)}^S$] and $oV_{2,1(lc)}^A$ [$pV_{2,1(lc)}^A$] are virtually indistinguishable and fall together the corresponding period times τ (and frequencies ω) are slightly different (inset in Fig. 3) due to variation in annihilation process. Corresponding PSDs and time evolutions of E_{kin} and η_{\pm} highlight the same frequencies (Figs. 10(1, 2) and 12(1, 2)). However, the PSD of E_{kin} for both asymmetric solutions, $oV_{2,1(lc)}^A$ (Fig. 10(1b)) and $pV_{2,1(lc)}^A$ (Fig. 12(1b)), highlights the double frequency 2ω (strongest/largest peak), corresponding to half a period $\tau/2$ indicating one process of vortex generation, motion and annihilation, either in upper or lower system half. The spacetime

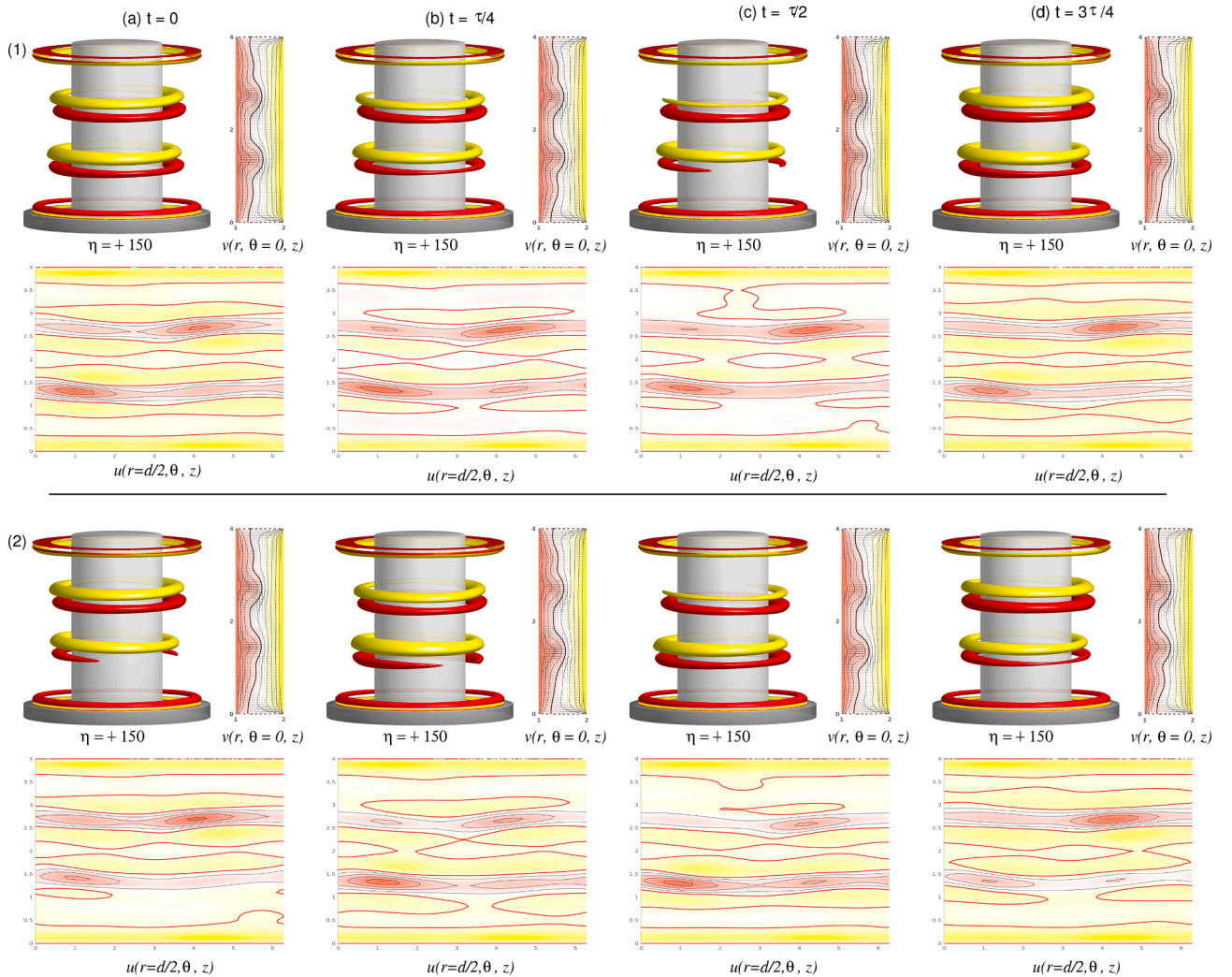


Fig. 9. Flow visualizations of oscillating flow structures $oV_{2,1(lc)}^S$ and $oV_{2,1(lc)}^A$ at $s_{xz} = 0.425$. Comparison of (1) $oV_{2,1(lc)}^S$ with period time $\tau \approx 0.148$ ($\omega \approx 6.739$) and (2) $oV_{2,1(lc)}^A$ with period time $\tau \approx 0.150$ ($\omega \approx 6.662$). Shown are over one period τ at instants of time (a) $t = 0$, (b) $t = \tau/4$, (c) $t = \tau/2$, and (d) $t = 3\tau/4$. For each time step are shown (clockwise) isosurfaces of η (isolevel shown at $\eta = \pm 150$). Vector plots $[u(r, z), w(r, z)]$ of the radial and axial velocity component $\theta = 0$, where the color-coded azimuthal velocity field v is also shown. Radial velocity $u(\theta, z)$ on an unrolled cylindrical surface in the annulus at mid-gap. Red (dark gray) and yellow (light gray) colors correspond to positive and negative values, respectively, with zero specified as white. [The same legends for flow visualization are used for all subsequent unsteady flows.] See also movies [movie_oVS21_sx0425.avi](#) and [movie_oVA21_sx0425.avi](#) in SM.

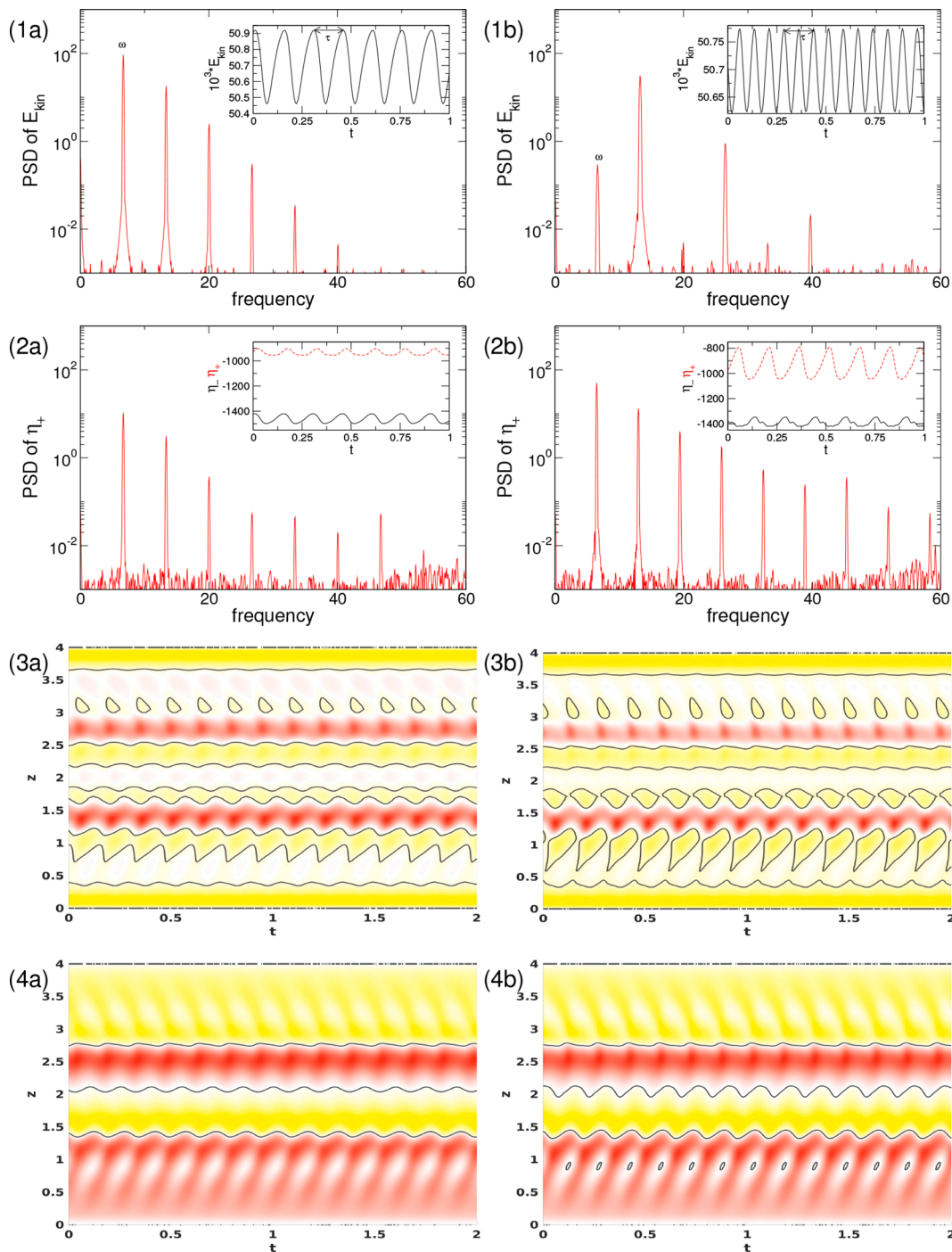


Fig. 10. Comparison of oscillating flow structures $oV_{2,1}^S$ and $oV_{2,1}^A$ at $s_{xz} = 0.425$. Shown are PSD of (1) E_{kin} , (2) η_+ (including insets illustrating corresponding time series) and spacetime plots of (3) $u(z, t)$ at $(r = d/2)$ and (4) $\eta(z, t)$ at $(r = r_i)$ of (a) $oV_{2,1}^S$ and (b) $oV_{2,1}^A$ at $s_{xz} = 0.425$. See also movies [movie_oVS21_sx0425.avi](#) and [movie_oVA21_sx0425.avi](#) in SM.

plots $u(z, t)$ at $(r = d/2)$ and $\eta(z, t)$ at $(r = r_i)$, show overall similar dynamics, which is more pronounced in case of the propagating time series) and spacetime plots of (3) $u(z, t)$ at $(r = d/2)$ and (4) $\eta(z, t)$ at $(r = r_i)$ of (a) $oV_{2,1}^S$ and (b) $oV_{2,1}^A$ at $s_{xz} = 0.425$. See also movies [movie_oVS21_sx0425.avi](#) and [movie_oVA21_sx0425.avi](#) in SM.

plots $u(z, t)$ at $(r = d/2)$ and $\eta(z, t)$ at $(r = r_i)$, show overall similar dynamics, which is more pronounced in case of the propagating time series) and spacetime plots of (3) $u(z, t)$ at $(r = d/2)$ and (4) $\eta(z, t)$ at $(r = r_i)$ of (a) $oV_{2,1}^S$ and (b) $oV_{2,1}^A$ at $s_{xz} = 0.425$. See also movies [movie_oVS21_sx0425.avi](#) and [movie_oVA21_sx0425.avi](#) in SM.

It is worth to mention, that the general dynamics for oscillating and propagating vortices under oblique magnetic field is moved towards the inner cylinder in comparison to the dynamics under pure axial or pure transversal magnetic field.

The difference in time evolution of η_{\pm} for $pV_{2,1}^S$ (for lc and $T2$) can be seen in corresponding time series (insets in Fig. 13) for different s_{xz} as indicated. Starting in the symmetric solution pV^S in absence of any

magnetic field time series of η_+ and η_- are identical and thus fall together (Fig. 13(1)). With increasing s_{xz} the time series separate indicating the loss of $Z_2^{H_x}$ symmetry. Aside the separation in absolute values, both time series are slightly shifted against each other, although the period τ itself basically remain the same for η_{\pm} (see Fig. 13(6)). The ‘peaks’ in time series η_{\pm} are slightly displaced. This results from the additional stimulated $m = 1$ modes, which destroy the symmetric appearance as they also do result in the different shape/dynamics η_{\pm} .

The PSDs of $pV_{2,1}^S$ in Fig. 13(1) shows the limit cycle topology having a single characteristic frequency. With finite value $s_{xz} \neq 0$ immediately

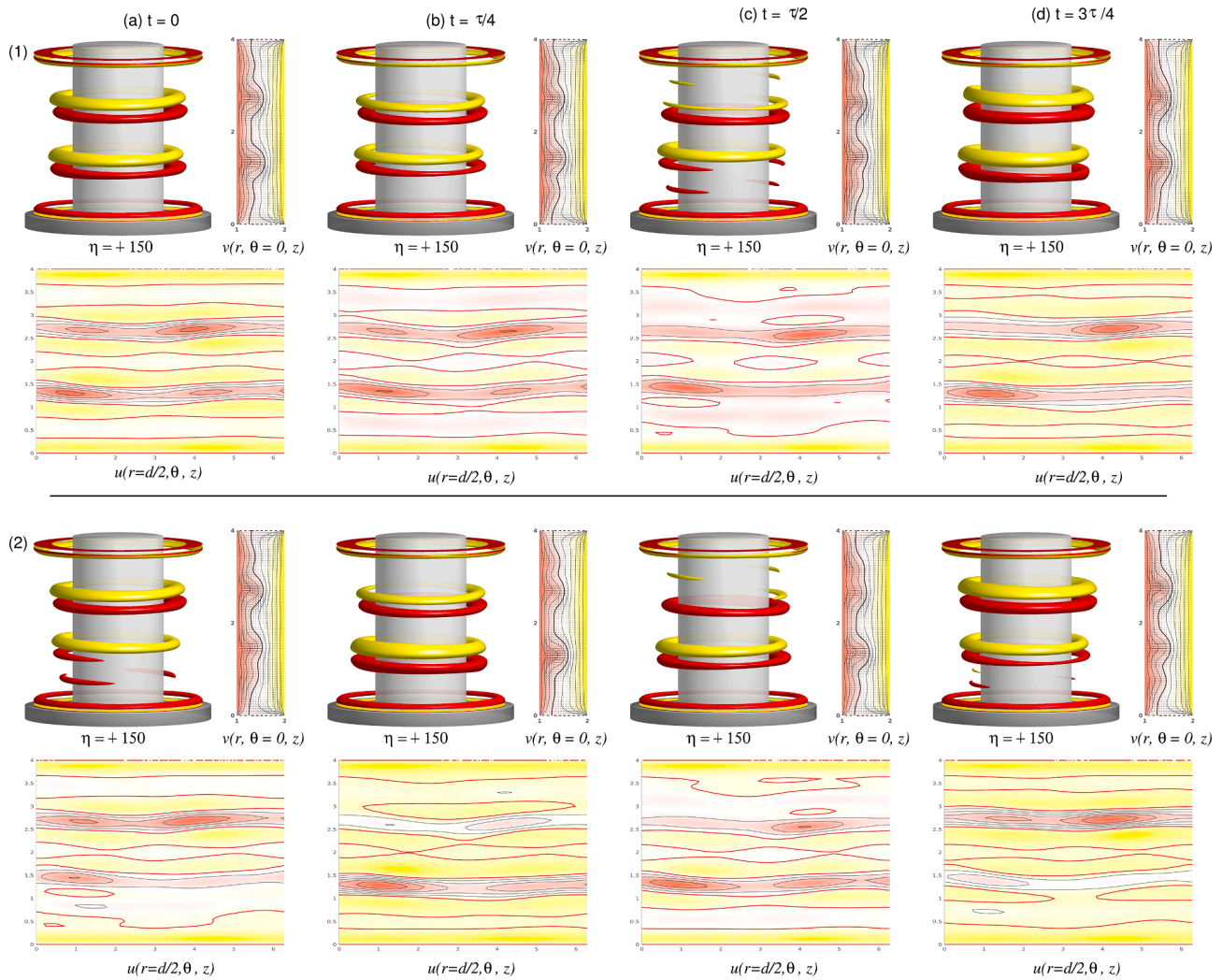


Fig. 11. Flow visualizations of propagating flow structures $pV_{2,1(lc)}^S$ and $pV_{2,1(lc)}^A$ at $s_{xz} = 0.4$. As Fig. 9 but at $s_{xz} = 0.4$ and comparison of (1) $pV_{2,1(lc)}^S$ with period time $\tau \approx 0.152$ ($\omega \approx 6.588$) and (2) $pV_{2,1(lc)}^A$ with period time $\tau \approx 0.154$ ($\omega \approx 6.515$). See also movies [movie_oVS21_sx04.avi](#) and [movie_oVA21_sx04.avi](#) in SM.

a second incommensurable frequency appears, which renders the flow to live on a 2-torus invariant manifold. As the global dynamics only smoothly change this frequency first appears in the PSD of local quantities η_{\pm} (Fig. 13(2b)) and becomes more and more pronounced for larger values s_{xz} . This second frequency, slightly changing with s_{xz} , appears to be about 1/3 of the dominant frequency ω .

This second frequency becomes more and more pronounced and present in PSDs of both, global quantity E_{kin} and local quantity η_{\pm} (Fig. 13(2–5)) before it finally disappears in the frequency locking at $s_{xz} \approx 0.33$ and therefore the flow changes back to be a limit cycle solution having only one single characteristic frequency (Fig. 13(6)).

3.3. (s_x, s_z) phase diagram

We will conclude our studies and investigations with the (s_x, s_z) phase diagram (Fig. 14) which covers the (s_x, s_z) parameter range investigated in both, the current and first part [37] investigating propagating vortex solutions. The bifurcation diagrams of Fig. 3 were obtained along the gray diagonal line $\eta_+ = \eta_-$. Corresponding bifurcation diagrams covering the scenario for either pure axial and pure transversal magnetic field were presented in Figs. 3 and 8 in [37] (i.e. axis in Fig. 14).

The blue line denotes the pitchfork bifurcation at which $oV_{2,1(lc)}^S$ (unstable) and $oV_{2,1(lc)}^A$ [$oV_{2,1(lc)}^*$] (stable) appear simultaneously out of the stationary solution $6V_{2,1}$. Note, that the basic state $CCF_{2,1}$ (cf. Fig. 3)

is out of the here presented parameter range. The table in the caption of Fig. 14 indicates the different regions with stable (s), unstable (u) and non existing (-) flow states. The lower boundaries of regions B and C indicate the smooth transition from the oscillating vortex solutions, $oV_{2,1(lc)}^S$ and $oV_{2,1(lc)}^A$, towards their propagating counterparts, $pV_{2,1(lc)}^S$ and $pV_{2,1(lc)}^A$, respectively.

The structure of the phase diagram in Fig. 14 can be summarized as follows: In region $F_{1,2}$ only the symmetric propagating vortices exist as stable solution. This is $pV_{2,1(2T)}^S$ in F_1 which changes to $pV_{2,1(lc)}^S$ in F_2 . While in region E, both, $pV_{2,1(lc)}^S$ and $pV_{2,1(lc)}^A$, are bistable coexisting, this change to the only stable solution $pV_{2,1(lc)}^A$ in region D. Increasing the magnetic field strength, s_x and/or s_z from region E into region C, either $pV_{2,1(lc)}^S$ and $pV_{2,1(lc)}^A$ undergo smooth transitions towards $oV_{2,1(lc)}^S$ and $oV_{2,1(lc)}^A$, respectively. Crossing from region C into region B, $oV_{2,1(lc)}^S$ loses stability with only $oV_{2,1(lc)}^A$ remaining as stable existing solution. In region A the stationary $6V_{2,1}$ solution is present, which appears out of the basic state $CCF_{2,1}$ at the larger control parameters s_x, s_z (cf. Fig. 3). Region G indicates the existence of the modulated solution $pV_{2,1}^{Am}$, which was discussed in more detail in [37].

The fact that the pitchfork bifurcation for pure axial field configuration appears at smaller (absolute value) field strength $s_z \approx 0.56$ in comparison to pure transversal field configuration with $s_x \approx 0.775$

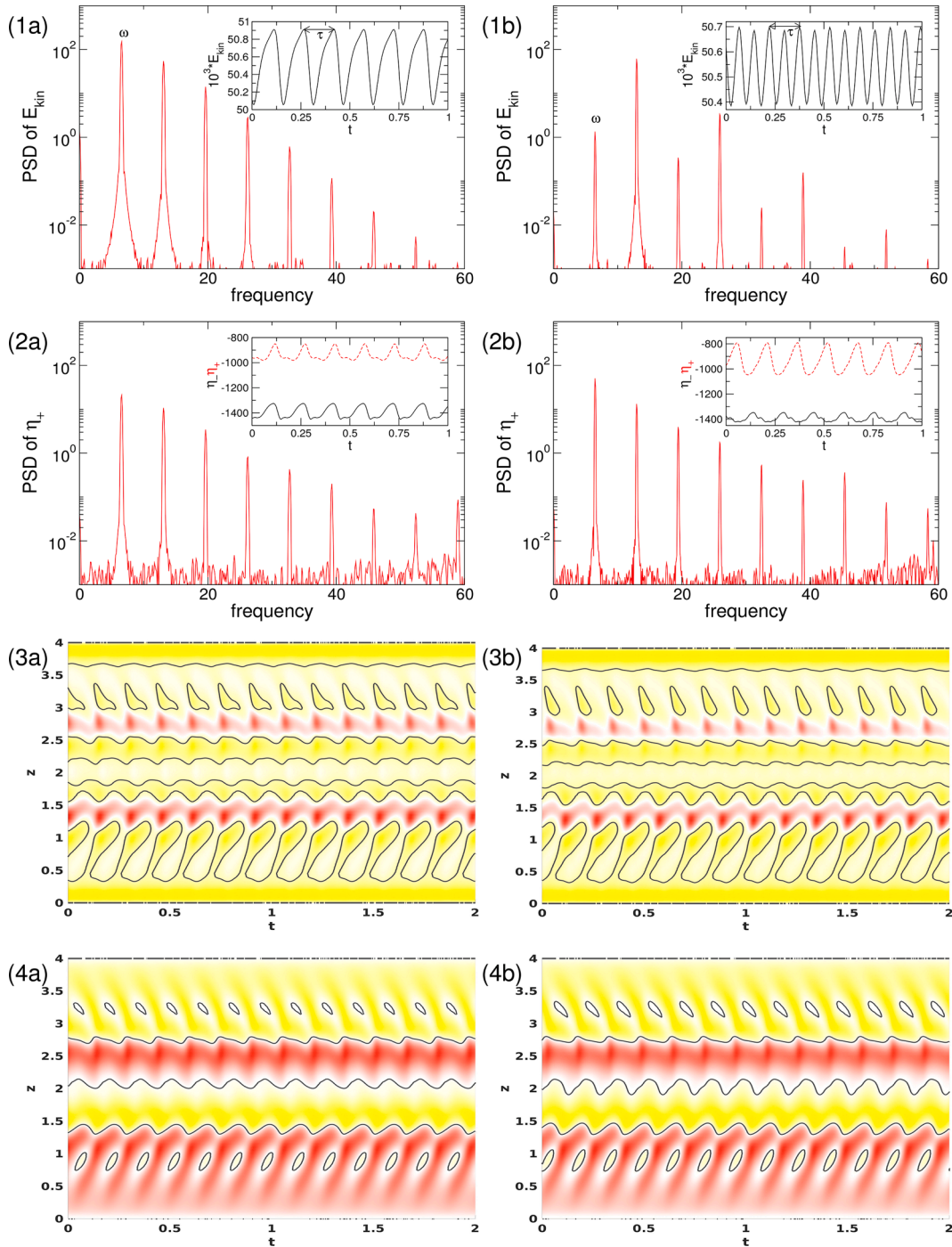


Fig. 12. Comparison of propagating flow structures $pV_{2,1(lc)}^S$ and $pV_{2,1(lc)}^A$ at $s_{xz} = 0.4$. As Fig. 10 but for $pV_{2,1(lc)}^S$ and $pV_{2,1(lc)}^A$ at $s_{xz} = 0.4$. See also movies [movie_pVS21_sx04.avi](#) and [movie_pVA21_sx04.avi](#) in SM.

highlights the well known larger stabilization effect of pure axial magnetic fields in comparison to pure transversal magnetic fields [35,8,9,37].

4. Discussion and conclusion

This paper is the second of two parts dealing with propagating vortices (pVs) in ferrofluidic Couette flow under influence of external magnetic field. While the first part dealt with pure magnetic fields, either pure axial or pure transversal (symmetry breaking) orientated, the current manuscript investigates the superposition of both axial and transversal, i.e. *oblique* magnetic fields. With changing (particular

decreasing) the magnetic field strength s_x and/or s_z symmetric solutions ($oV_{2,1(lc)}^S$) as well as asymmetric ones ($oV_{2,1(lc)}^{A*}$) appear in a symmetry breaking pitchfork bifurcation. Due to any transversal, symmetry breaking component all flow states are inherently 3D [7] and in combination with the axial field, all flow solutions have a finite $m = 1$ mode under oblique field configuration.

Similar to pure transversal magnetic field, close to onset only the asymmetric solutions appear stable, while symmetric ones are unstable [37]. However, for oblique field configuration the initial appearing solutions are only *oscillating* and *non-propagating* flow structures. This holds for both, symmetric and asymmetric ones ($oV_{2,1(lc)}^S$, $oV_{2,1(lc)}^A$)

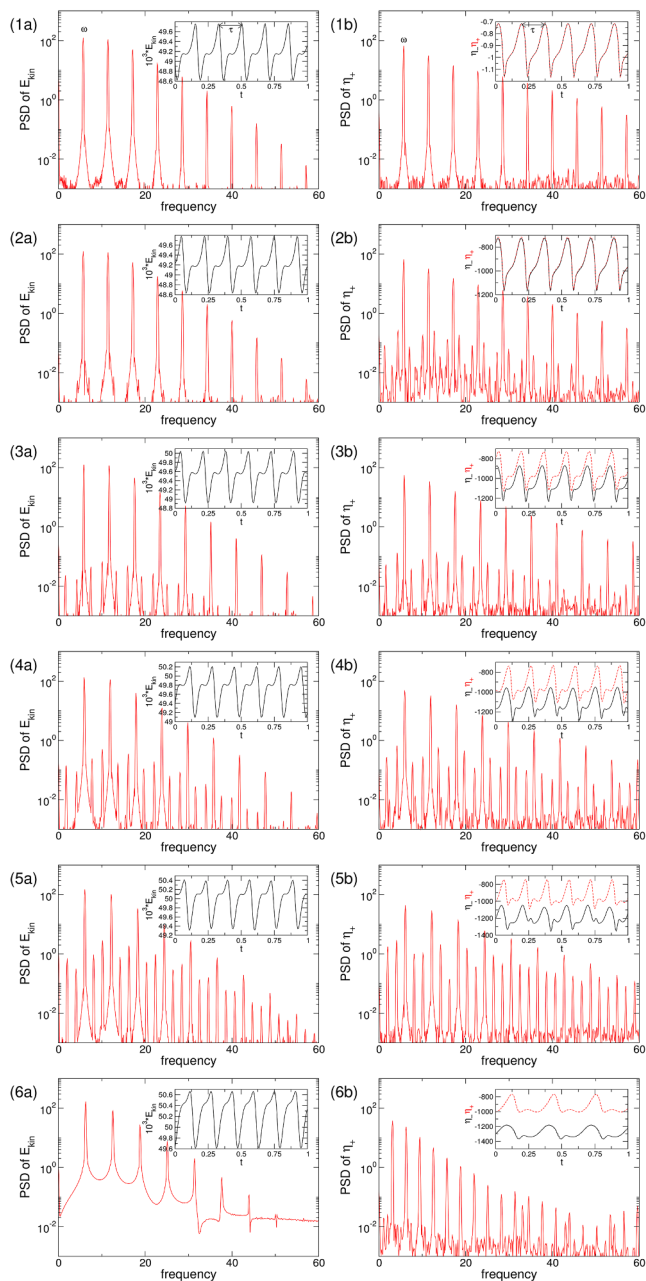


Fig. 13. Power spectral densities (PSDs) of (a) E_{kin} and (b) η_+ for different $pV_{2,1(2T)}^S$. (1) In absence of any magnetic field (cf. Figs. 1 and 4(a) in [37]) with period time $\tau \approx 0.173$ and corresponding frequency $\omega \approx 5.779$. (2) For $s_{xz} = 0.05$ with period time $\tau \approx 0.173$ and corresponding frequency $\omega \approx 5.779$. (3) For $s_{xz} = 0.2$ with period time $\tau \approx 0.169$ and corresponding frequency $\omega \approx 5.926$. (4) For $s_{xz} = 0.25$ with period time $\tau \approx 0.167$ and corresponding frequency $\omega \approx 5.999$. (5) For $s_{xz} = 0.3$ with period time $\tau \approx 0.163$ and corresponding frequency $\omega \approx 6.147$. (6) For $pV_{2,1(lc)}^S$ $s_{xz} = 0.35$ with period time $\tau \approx 0.319$ and corresponding frequency $\omega \approx 3.132$. Insets show time series of E_{kin} , η_+ [red], η_- [black]. For $pV_{2,1(2T)}^S$ at $s_x = 0.3$ see also movie [movie_pVA21_sxz03.avi](#) in SM.

equally. With decreasing the magnetic field strength these oscillating solutions undergo a smooth transition into propagating vortex states ($pV_{2,1(lc)}^S$, $pV_{2,1(lc)}^A$). Although symmetric and asymmetric states being indistinguishable in the time-averaged modal kinetic energy, they have an observable difference in their corresponding period times. This time is larger for the asymmetric states resulting from complexer annihilation processes in the central defect region based on the alternating

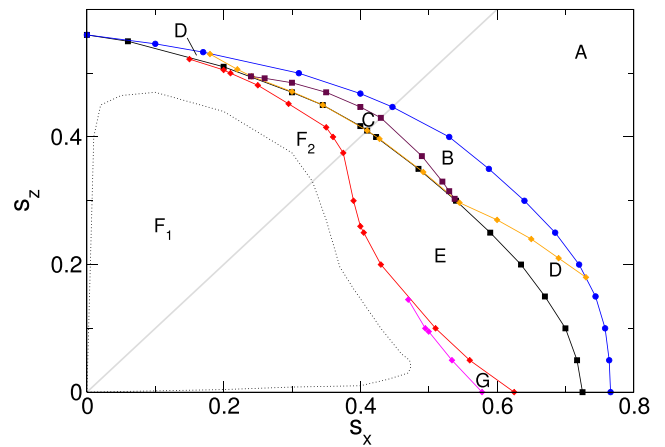


Fig. 14. Phase diagram for oV and pV solutions in (s_x, s_z) -plane. The diagonal $s_x = s_z$ indicate the parameter range of the bifurcation diagrams of Fig. 3. Corresponding bifurcation diagrams for either pure axial and pure transversal magnetic fields have been presented in the first part of this study [37] in Figs. 3 and 8, respectively.

annihilation of vortices.

In contrast to all former studied and described pVs in literature, existing as periodic states and therefore characterized as limit cycle solutions [37,10,35], the pVs under oblique magnetic fields are found to be periodic or only quasi-periodic depending on different system parameters. Therefore they exist on either one dimensional (as all former known) or two dimensional invariant manifolds, which renders them to be limit cycle (1-torus) $pV_{2,1(lc)}^S$ or 2-tori solutions $pV_{2,1(2T)}^S$. While being intrinsically 2-tori solutions changing the field strength (s_x, s_z) as control parameter we detected frequency locking resulting in simpler limit cycle solutions (1-torus) again.

Worth to mention, although this study for different external magnetic fields, shed further light on the parameter range in which pVs appear stable as well as unstable and their underlying topology, the huge number of control parameters in TCS still leaves many open gaps which should be motivation for future exploration. In particular we hope to motivate experimental studies as the here considered parameters are very well achievable. Moreover, the here detected underlying topology of pV states to exist either as limit cycle (1-torus) and 2-torus solutions in presence of oblique magnetic fields may be only the ‘top of the iceberg’ and further experimental and numerical studies will have to be undertaken in this field.

CRedit authorship contribution statement

Sebastian Altmeyer: Conceptualization, Methodology, Software, Data curation, Writing - original draft, Visualization, Investigation, Validation, Writing - review & editing.

Declaration of Competing Interest

The authors declare that they have no known competing financial interests or personal relationships that could have appeared to influence the work reported in this paper.

Acknowledgments

S. A. is a Serra Hünter Fellow.

Appendix A. Supplementary data

Supplementary data associated with this article can be found, in the online version, at <https://doi.org/10.1016/j.jmmm.2021.167788>.

References

- [1] G.I. Taylor, Stability of a viscous liquid contained between two rotating cylinders, *Philos. Trans. R. Soc. London A* 223 (1923) 289.
- [2] S. Chandrasekhar, *Hydrodynamic and Hydromagnetic Stability*, Dover, New York, 1981.
- [3] R.C. DiPrima, H.L. Swinney, Instabilities and transition in flow between concentric rotating cylinders, in: H.L. Swinney, J.G. Gollub (Eds.), *Hydrodynamic Instabilities and the Transition to Turbulence*, number 45 in *Topics in Applied Physics*, Springer, Berlin, 1985.
- [4] P. Chossat, G. Iooss, *The Couette-Taylor Problem*, Springer, Berlin, 1994.
- [5] R. Tagg, The Couette-Taylor Problem, *Nonlinear Sci. Today* 4 (1994) 1.
- [6] C.D. Andereck, S.S. Liu, H.L. Swinney, Flow regimes in a circular Couette system with independently rotating cylinders, *J. Fluid Mech.* 164 (1986) 155.
- [7] S. Altmeyer, C. Hoffmann, A. Leschhorn, M. Lücke, Influence of homogeneous magnetic fields on the flow of a ferrofluid in the Taylor-Couette system, *Phys. Rev. E* 82 (2010), 016321.
- [8] M. Reindl, S. Odenbach, Influence of a homogeneous axial magnetic field on Taylor-Couette flow of ferrofluids with low particle-particle interaction, *Expts. Fluids* 50 (2011) 375.
- [9] M. Reindl, S. Odenbach, Effect of axial and transverse magnetic fields on the flow behavior of ferrofluids featuring different levels of interparticle interaction, *Phys. Fluids* 23 (2011), 093102.
- [10] T. Ilzig, K. Stöckel, S. Odenbach, Experimental Investigations on the Effect of Axial Homogenous Magnetic Fields on Propagating Vortex Flow in the Taylor-Couette System, *Materials* 12 (2019) 4027.
- [11] S. Altmeyer, A. Leschhorn, C. Hoffmann, M. Lücke, Elongational flow effects on the vortex growth out of Couette flow in ferrofluids, *Phys. Rev. E* 87 (2013), 053010.
- [12] S. Altmeyer, J. Lopez, Y. Do, Influence of an inhomogeneous internal magnetic field on the flow dynamics of ferrofluid between differentially rotating cylinders, *Phys. Rev. E* 85 (2012), 66314.
- [13] S. Altmeyer, J. Lopez, Y. Do, Effect of elongational flow on ferrofluids under a magnetic field, *Phys. Rev. E* 88 (2013), 013003.
- [14] S. Altmeyer, Y.-H. Do, Y.-C. Lai, Transition to turbulence in Taylor-Couette ferrofluidic flow, *Sci. Rep.* 5 (2015) 10781.
- [15] S. Altmeyer, Y.-H. Do, Y.-C. Lai, Magnetic field induced flow reversal in a ferrofluidic Taylor-Couette system, *Sci. Rep.* 5 (2015) 18589.
- [16] S. Altmeyer, *Pattern Formation and Stability in Magnetohydrodynamics - Interaction of Magnetic Fields on Ferrofluidic Taylor-Couette Flow*. IntechOpen.
- [17] A. Leschhorn, M. Lücke, C. Hoffmann, S. Altmeyer, Stability of circular Couette flow of a ferrofluid in an axial magnetic field: Influence of polydispersity, *Phys. Rev. E* 79 (2009), 036308.
- [18] S. Altmeyer, Non-linear dynamics and alternating 'flip' solutions in ferrofluidic Taylor-Couette flow, *J. Magn. Magn. Mater.* 452 (2018) 427.
- [19] S. Altmeyer, Y.-H. Do, Y.-C. Lai, Dynamics of ferrofluidic flow in the Taylor-Couette system with a small aspect ratio, *Sci. Rep.* 7 (2017) 40012.
- [20] M.I. Shliomis, Effective Viscosity of Magnetic Suspensions, *Sov. Phys. JETP* 34 (1972) 1291-1294.
- [21] R.E. Rosensweig, *Ferrohydrodynamics*, Cambridge University Press, Cambridge, 1985.
- [22] T. Benjamin, Bifurcation phenomena in steady flows of a viscous fluid. I. Theory. *Philos. Trans. Roy. Soc. A* p. 1 (1978).
- [23] T. Benjamin, Bifurcation phenomena in steady flows of a viscous fluid. II. Experiments. *Philos. Trans. Roy. Soc. A* p. 27 (1978).
- [24] G. Pfister, H. Schmidt, K.A. Cliffe, T. Mullin, Bifurcation phenomena in Taylor-Couette flow in a very short annulus, *J. Fluid Mech.* 191 (1988) 1.
- [25] A. Lorenzen, G. Pfister, T. Mullin, End effects on the transition to time-dependent motion in the Taylor experiment, *Phys. Fluids* 26 (1983) 10.
- [26] K.A. Cliffe, J.J. Kobine, T. Mullin, The role of anomalous modes in Taylor-Couette flow, *Philos. Trans. Roy. Soc. A* 439 (1992) 341.
- [27] S. Altmeyer, C. Hoffmann, M. Heise, J. Abshagen, A. Pinter, M. Lücke, G. Pfister, End wall effects on the transitions between Taylor vortices and spiral vortices, *Phys. Rev. E* 81 (2010), 066313.
- [28] M. Golubitsky, I. Stewart, *Symmetry and Stability in Taylor-Couette flow*, *SIAM J. Math. Ana.* 17 (1986) 249.
- [29] M. Golubitsky, W.F. Langford, Pattern formation and bistability in flow between counterrotating cylinders, *Physica D* 32 (1988) 362.
- [30] J. Linke, S. Odenbach, Anisotropy of the magnetoviscous effect in a cobalt ferrofluid with strong interparticle interaction, *J. Magn. Magn. Mater.* 396 (2015) 85.
- [31] C. Hoffmann, M. Lücke, *Spiral vortices and Taylor vortices in the annulus between counter-rotating cylinders*, Springer Verlag, Berlin, 2000, p. 55.
- [32] M. Nagata, On wavy instabilities of the Taylor-vortex flow between corotating cylinders, *J. Fluid Mech.* 88 (1988) 585.
- [33] S.T. Wereley, R.M. Lueptow, Spatio-temporal character of non-wavy and wavy Taylor-Couette flow, *J. Fluid Mech.* 364 (1988) 59.
- [34] C.A. Jones, The transition to wavy Taylor vortices, *J. Fluid Mech.* 175 (1985) 135.
- [35] C. Hoffmann, S. Altmeyer, M. Heise, J. Abshagen, G. Pfister, Axisymmetric propagating vortices in centrifugally stable Taylor-Couette flow, *J. Fluid Mech.* 728 (2013) 458.
- [36] J. Abshagen, M. Heise, G. Pfister, T. Mullin, Multiple localized states in centrifugally stable rotating flow, *Phys. Fluids* 22 (2010), 021702.
- [37] S. Altmeyer, *Propagating vortices in ferrofluidic Couette flow under magnetic fields - part I: axial and symmetry breaking transversal orientated fields*. under review.
- [38] I. Nakamura, Z. Toya, *Acta Mech.* 117 (1996) 33.
- [39] T. Buzug, J. von Stamm, G. Pfister, Characterization of experimental time series from taylor-couette flow, *Physica A* 191 (1992) 559.
- [40] M. Niklas, Influence of magnetic fields on Taylor vortex formation in magnetic fluids.
- [41] H.W. Müller, M. Liu, Structure of ferrofluid dynamics, *Phys. Rev. E* 64 (2001), 061405.
- [42] S. Odenbach, H.W. Müller, On the microscopic interpretation of the coupling of the symmetric velocity gradient to the magnetization relaxation. *J. Magn. Magn. Mater.* 289 242 (2005) *Z. Phys. B* 68, 493 (1987).
- [43] J.P. McTague, Magnetoviscosity of magnetic colloids, *J. Chem. Phys.* 51 (1969) 133.
- [44] R.E. Rosensweig, R. Kaiser, G. Miskolczy, Magnetoviscosity of magnetic fluid in a magnetic field, *J. Colloid Interface Sci.* 29 (1969) 680.
- [45] P. Langevin, Magnétisme et théorie des électrons, *Annales de Chemie et de Physique* 5 (1905) 70.
- [46] O. Ambacher, S. Odenbach, K. Stierstadt, Rotational viscosity in ferrofluids, *Z. Phys. B* 86 (1992) 29.
- [47] C. Hoffmann, M. Heise, S. Altmeyer, J. Abshagen, A. Pinter, G. Pfister, M. Lücke, Nonlinear defects separating spiral waves in Taylor-Couette flow, *Phys. Rev. E* 80 (2009), 066308.